Solar Energy Materials & Solar Cells 223 (2021) 110972

Contents lists available at ScienceDirect

Solar Energy Materials and Solar Cells

journal homepage: http://www.elsevier.com/locate/solmat

Monte-Carlo optical model coupled with Inverse Adding-Doubling for Building Integrated Photovoltaic smart window design and characterisation

Xiao Liu , Yupeng Wu *

Department of Architecture and Built Environment, Faculty of Engineering, The University of Nottingham, University Park, Nottingham, NG7 2RD, United Kingdom

ARTICLE INFO

Keywords:
Building integrated photovoltaic
Smart window
Thermotropic membrane
Scattering
Monte-carlo ray-tracing
Inverse adding-doubling

ABSTRACT

Building Integrated Photovoltaic (BIPV) glazings are promising technologies with the benefits of electricity generation, solar shading and building energy savings. A new approach is to integrate BIPV windows with thermotropic materials such as Hydroxypropyl Cellulose (HPC) hydrogel, which offers adaptive advantages for the systems to respond to time-varying weather conditions but also enhances the PV electricity generation. To design such systems, knowledge of the temperature-dependent scattering properties of the selected thermotropic materials is of significance. In this study, a Building Integrated Photovoltaic (BIPV) smart window system consisting of a thermotropic membrane synthesised using HPC and gellan gum gelling agent for electricity generation and also solar control has been designed and investigated. An advanced optical model, which combines a Monte-Carlo ray-tracing technique with an Inverse Adding-Doubling (IAD) method, has been developed for characterising the thermotropic membrane in terms of angular scattering distribution under various membrane temperatures and HPC concentrations. Then the developed optical model has been validated by comparison with experimental measurements. Subsequently, the validated optical model has been used to design and optimise the proposed BIPV smart window. The effects of HPC concentration, geometric concentration ratio, thermotropic membrane thickness and glass refractive index on PV power outputs have been evaluated. Finally, a prototype of the BIPV smart window with a 6 wt% HPC membrane has been manufactured and tested under indoor conditions. From the experimental tests, it was found that the total transmittance of the double-pane glass sample with a 6 wt% HPC membrane layer decreases from approximately 90%to 14%, when the membrane temperature increases from 27 °C to 56 °C. The measured short-circuit current for the prototype BIPV smart window is up to 1.15 times higher than that of its counterpart system with a similar PV area but no membrane.

1. Introduction

Harnessing solar energy to generate electricity based on Building Integrated Photovoltaics (BIPV) systems is a promising solution leading towards green and sustainable buildings. In such systems, Photovoltaic (PV) cells replace conventional building materials and serve as a part of the building envelopes providing savings in materials, generating electricity on site as well as protecting buildings from weather (e.g. shading and thermal insulation) [1,2]. In recent years, it has becoming increasingly popular to integrate Concentrating Photovoltaics (CPVs) into building windows or glazed façades to offer electricity and aesthetically pleasing features to buildings [3]. Given the flexibility in the shape and dimensions of concentrating optics, ray-tracing technique has usually been applied for BICPV system design and optical characterisation [4,5]. For example, Kerrouche et al. [6] investigated a Luminescent Solar Concentrator (LSC) based stained glass window using ray-tracing simulations. The prediction results show that the LSC enables light over a wide range of incidence angles to be collected around the window edges where solar cells are attached and the maximum optical efficiency is approximately 6%. Sellami et al. [7] designed a BICPV window consisting of dielectric-filled solar concentrators with a Square Elliptical Hyperboloid (SEH) profile. The optical efficiency was predicted to be in the range of 30–68% for the SEH concentrator with a geometric concentration ratio varying between 4 and 10. Shanks et al. [8] studied a BICPV window based on Cross Compound Parabolic Concentrators (CCPCs). Different optical efficiencies and PV power outputs were observed for the CCPCs made from different dielectric materials. Kim et al. [9] predicted the performance of a flat-plate CPV system comprised of a BK7 glass plate with its rear surface roughened to form a diffuser, which was assumed as a Lambertian-type diffused

* Corresponding author.
E-mail address: Yupeng.Wu@nottingham.ac.uk (Y. Wu).

https://doi.org/10.1016/j.solmat.2021.110972
Received 21 November 2020; Received in revised form 6 January 2021; Accepted 7 January 2021
Available online 26 January 2021

reflector for the optical modelling. Wu et al. [10] proposed a BICPV smart window with a thermotropic (TT) reflective layer for dynamic modulation of incident solar radiation. It was assumed that in the optical simulation, the TT layer in its translucent state behaves as a Lambertian reflector reflecting light equally into all directions. However, in practice, the light reflection from a translucent medium with a slab geometry is anisotropic in almost all situations [11]. The simple ray-tracing technique applied in the previous studies might not be accurate enough to predict the optical performance of a solar system when a translucent medium is involved. Therefore, a model considering the non-Lambertian scattering with angular distribution is required.

Typically, the light distribution in a diffuse medium can be modelled based on its intrinsic optical properties, including absorption coefficient (μ_a), scattering coefficient (μ_s), anisotropy factor (g) and reduced scattering coefficient (μ_s') [12–15]. These volume scattering properties can be estimated by the direct methods and the inverse methods [12,16,17]. In the direct methods (e.g. Lorenz-Mie theory), the physical properties of a diffuse medium and its constituent particles, such as refractive index, particle size, shape and concentration, are measured with specialised equipment and used as input in Maxwell's equations to yield solutions for the volume scattering properties [17–19]. If these experimental data are not available, the volume scattering properties can be estimated by the Inverse or fitting approaches, such as the Kubelka-Munk method [20], the diffusion approximation [21] and the Inverse Adding-Doubling (IAD) method [19]. The prerequisites for these inverse methods are the macroscopic quantities of a diffuse medium, such as reflectance and transmittance, which can be obtained using the experimental setups such as integrating spheres and goniometers [18].

The IAD method is regarded as a standard reference approach to estimate the volume scattering properties of diffuse media, with advantages such as fast computation, good flexibility and broad applicability [14,16]. In the IAD method, an initial guess is made for the volume scattering properties of a sample. The guessed values are used for calculating the sample's reflectance and transmittance with the Adding-Doubling (AD) method, and iteratively adjusted until a good fit between the calculated and measured values is obtained. The IAD method applies to any diffuse medium for which the Radiative Transport Equation (RTE) is valid, and places no restrictions on albedo, optical depth and scattering anisotropy [22,23]. Typically, three input variables are required for the IAD calculation: the total reflectance, total transmittance and collimated transmittance of a diffuse medium. These data are usually available from the measurement with a single/double integrating sphere system [14,24] or a Bi-directional Scattering Distribution Function (BSDF) device [15,18,19].

The IAD method has been used to investigate the light scattering in a host of diffuse media such as fruit and vegetable tissues [14,25,26], tissue-mimicking phantoms for clinic use [23,27,28], translucent liquids [12,19] and plastic diffusers [19,29]. Leyre et al. [19] used the IAD method to estimate the volume scattering properties for a concentration series of diluted milk in glass cuvettes, which were used as input to Monte-Carlo ray-tracing simulations to predict the angular scattering intensity distribution of the samples with different milk concentrations and thicknesses. Good agreement was obtained between the simulated results and the data measured using a BSDF device. Xie et al. [30] investigated the optical characteristics of Quantum dots (QDs)-Polymethyl methacrylate (PMMA) films by using a combination of IAD calculation and double-integrating-sphere measurement. It was found that the QDs-PMMA films exhibit stronger scattering and absorption at higher QDs concentrations and for the incident laser with a lower wavelength.

In this study, a Building Integrated PV (BIPV) smart window system consisting of a Hydroxypropyl Cellulose (HPC) based thermotropic

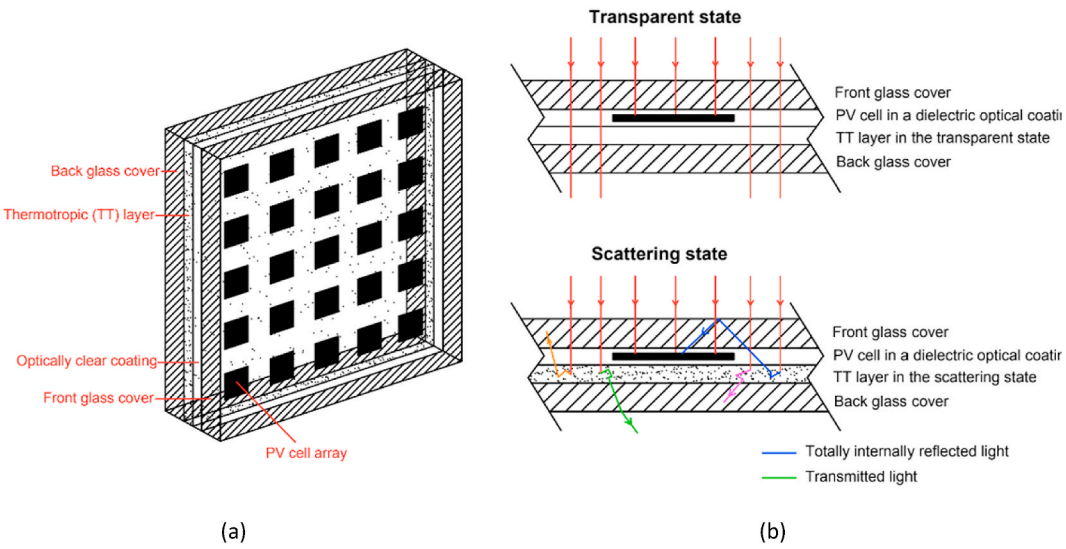

Fig. 1. (a) Schematic diagram of the BIPV smart window system and (b) possible light paths in the system.

membrane layer has been designed for electricity generation and adaptive daylighting control. The schematic diagrams are shown in Fig. 1. In principle, the thermotropic layer automatically responds to its temperature change, by varying the proportion of solar radiation transmitted through it and reflected from it. In the transparent state (Fig. 1(b) top diagram), on a cool day, some of the solar radiation falls on the front-face solar cells for electricity generation, and the rest penetrates through the window for building daylighting and passive heating. In the light-scattering state (Fig. 1(b) bottom diagram), on a warm day, a proportion of the light backscattered from the thermotropic membrane is redirected through Total Internal Reflection (TIR) towards the solar cells for electricity generation in addition to the light directly incident on the cell surfaces. Meanwhile, the light scattering effect potentially can protect the indoor environment from excessive solar heat gain and glare, thus reducing the energy consumption for space cooling and artificial lighting in buildings. To accurately represent the dynamic scattering behaviour of the HPC based thermotropic membrane, an advanced optical model that combines a Monte-Carlo ray-tracing technique with an IAD method has been developed and validated. In this model, the IAD has been used to determine the volume scattering properties of the thermotropic membrane. This developed optical model has been subsequently used to optimise the BIPV smart window design, where the effects of HPC concentration, geometric concentration ratio, thermotropic membrane thickness and glass refractive index on PV power outputs have been evaluated. Finally, a prototype has been developed and characterised.

2. Advanced optical model

A flow chart showing the procedure of the development and validation of the proposed advanced optical model is illustrated in Fig. 2. At first, the total reflectance (R_t), total transmittance (T_t) and collimated transmittance (T_c) of a thermotropic laminated glazing sample (4-mm-thick glass pane/1-mm-thick 2 wt% HPC based thermotropic membrane layer/4-mm-thick glass pane) were measured and used as input to an IAD algorithm. The volume scattering properties of the thermotropic membrane, including absorption coefficient (μ_a), reduced scattering coefficient (μ_s') and anisotropy factor (g), were derived from the IAD calculation and then imported into a Monte-Carlo ray-tracing model. The intensities of light transmitted through the thermotropic laminated glazing sample observed at multiple scattering angles ($G_{sim}(\theta)$) were simulated with the Monte-Carlo ray-tracing technique and compared to experimental data ($G_{exp}(\theta)$). To gain deeper insight into the thermotropic membrane performance, its angular scattering profile and spatial flux distribution were simulated under varying membrane temperatures and HPC concentrations. The developed model was subsequently used for the design and optimisation of the proposed BIPV smart window system. The simulated results for the optimised prototype were compared to the data obtained from an indoor experiment, as further validation of the developed numerical method for BIPV and smart window applications.

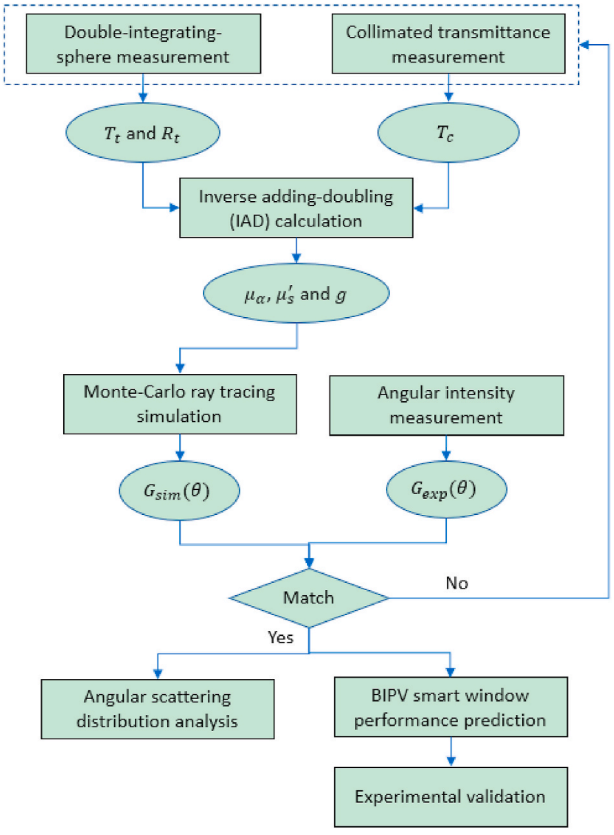

Fig. 2. Flow chart presenting the process for optical simulation and validation.

2.1. Optical measurements

The thermotropic membranes were synthesised using HPC polymer and Gellan Gum type F (GGF) gelling agent. The detailed synthesis procedures can be found in our previously published paper by Connelly et al. [31]. The total reflectance (R_t) and total transmittance (T_t) of a laminated glazing sample with an HPC-GGF thermotropic membrane layer were measured using a double-integrating-sphere (DIS) system illustrated in Fig. 3(a). In the DIS system, the totally reflected light (including the specularly and diffusely reflected light) from the sample was collected by an Ocean Optics ISP-REF integrating sphere; and the totally transmitted light (including the specularly and diffusely transmitted light) through the sample was collected by an Ocean Optics FOIS-1 integrating sphere. The spheres were connected to an Ocean Optics USB2000+UV-VIS-ES spectrometer via 400 μm core diameter optical fibres. The collimated transmittance (T_c) of the sample, which is defined as the light transmitted through the sample without being scattered [17,24], was measured using the setup illustrated in Fig. 3(b). A collimated detector consisting of an Ocean Optics 74-UV collimating lens and a 400 μm core diameter optical fibre was positioned at a distance of 20 cm from the sample with its centre aligned with the incident beam. The collimated detector was connected to the Ocean Optics USB2000+UV-VIS-ES spectrometer. A distance independence test has been conducted for the collimated transmittance measurement. As can be seen from Fig. 4, the measured collimated transmittance decreases exponentially with increasing the distance between the sample and detector, indicating less diffuse light being detected. No significant decrease in collimated transmittance has been observed when the distance is over 20 cm.

Before the optical measurements, a GyroStir-DH hotplate was used to heat the thermotropic membrane to a defined temperature with an equilibrium time of at least 10 min. The membrane temperature was recorded and monitored by a T-type thermocouple embedded in the membrane (see Fig. 5) and connected to a DT85 data taker. The uniformity of temperature distribution across the membrane was checked by using a FLIR E40BX infrared camera. The thermal and optical measurements were repeated at least triplicate, to account for the uncertainty due to membrane temperature fluctuation.

2.2. IAD calculation and ray-tracing simulation

The measured spectral data of R_t, T_t and T_c were imported to an IAD algorithm [24,32,33], with which μ_a, μ_s' and g as a function of wavelength were calculated [26,34]. A flow chart of the IAD algorithm is shown in Fig. 6. The additional input parameters for the IAD calculation include the average refractive index of the low-iron optical glass panes

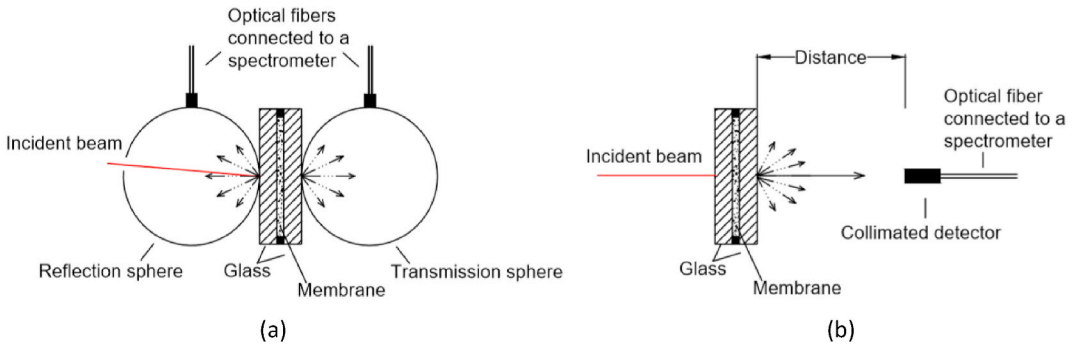

Fig. 3. (a) Double-integrating-sphere system and (b) collimated transmittance measurement setup.

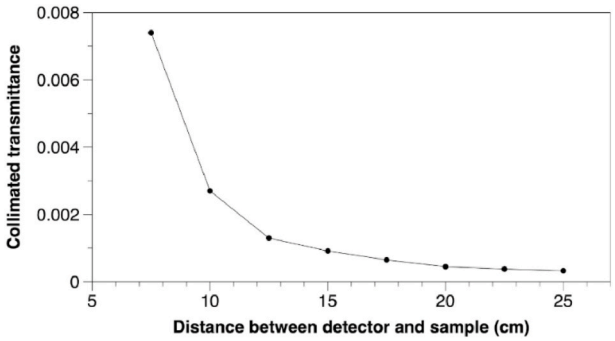

Fig. 4. Measured collimated transmittance of the sample with a 2 wt% HPC, 1.5 wt% GGF based TT membrane in the translucent state against sample-detector distance.

(1.51), the average reflective index of the thermotropic layer (1.34), the glass pane thickness (4 mm), the thermotropic layer thickness (1 mm), the illumination beam diameter (1.5 mm), the diameters of the integrating spheres (38 mm), the diameters of the sample ports (10 mm) and the sphere wall reflectivity (98%). In the IAD algorithm, the refractive indices of the glass panes and thermotropic layer are used to calculate the Fresnel reflection at boundaries, and the geometrical dimensions are used to correct the light loss when using the DIS measurement setup [24]. The refractive index of 2 wt% HPC aqueous solution is 1.34 according to the literature [35,36] and is considered as the refractive index of the thermotropic layer under study.

A Monte-Carlo ray-tracing model has been developed to simulate the optical characteristics of the thermotropic laminated glazing sample. The light propagation in the thermotropic layer was approximated using its absorption coefficient μ_a, scattering coefficient μ_s (given by Eq. (1) [34]) and single-scattering phase function $p(\theta)$ as input. μ_a (or μ_s) is defined as the reciprocal of the average free path that light travels between two absorption (or scattering) events [12,30]. The single-scattering phase function describes the fraction of light scattered at an angle θ from the incident direction after a single scattering event [12,16]. In this work, the Henyey–Greenstein phase function with a single variable g (anisotropy factor) was implemented for the simulation, given by Eq. (2) [34]. Other input parameters include the refractive index and absorption coefficient of the low-iron optical glass panes, the refractive index of the thermotropic layer, the measured irradiation intensity of the light source and the number of incident rays where 1, 000,000 rays were used in this study confirmed through a ray independence test.

2.3. Validation of the optical models

The optical model was validated by an experiment using the setup shown in Fig. 7. A laminated glazing sample comprised of a thermotropic layer (40 mm × 40 mm × 1 mm) between two optical glass covers (50 mm × 50 mm × 4 mm) was mounted in the centre of a rotation device. The sample was illuminated by a collimated light source that consists of an Ocean Optics 74-UV collimating lens, a 400 μm core diameter optical fibre and an Ocean Optics HL2000 tungsten halogen lamp. The normal incident beam has a diameter of 5 mm and a total irradiation intensity of 36 W/m^2 across the 350–1000 nm spectrum. A detector (at a 10 cm distance from the centre and 15 cm away from the light source) moved around the sample to collect the light scattered at a predefined set of angles. The detector consists of an Ocean Optics CC-3-UV-S cosine corrector (with an aperture diameter of 3.9 mm and a field of view 180°) and a 400 μm core diameter optical fibre connected to an Ocean Optics USB2000+UV-VIS-ES spectrometer. The optical detection system had been calibrated for absolute spectral irradiance against an

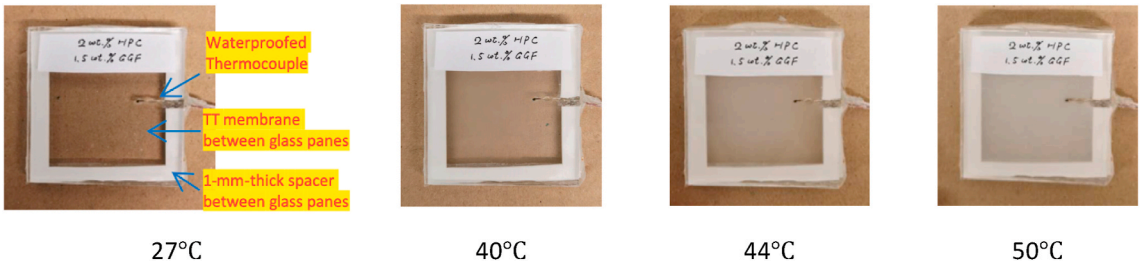

Fig. 5. Images illustrating the states of the sample with a 2 wt% HPC, 1.5 wt% GGF based TT membrane at different temperatures.

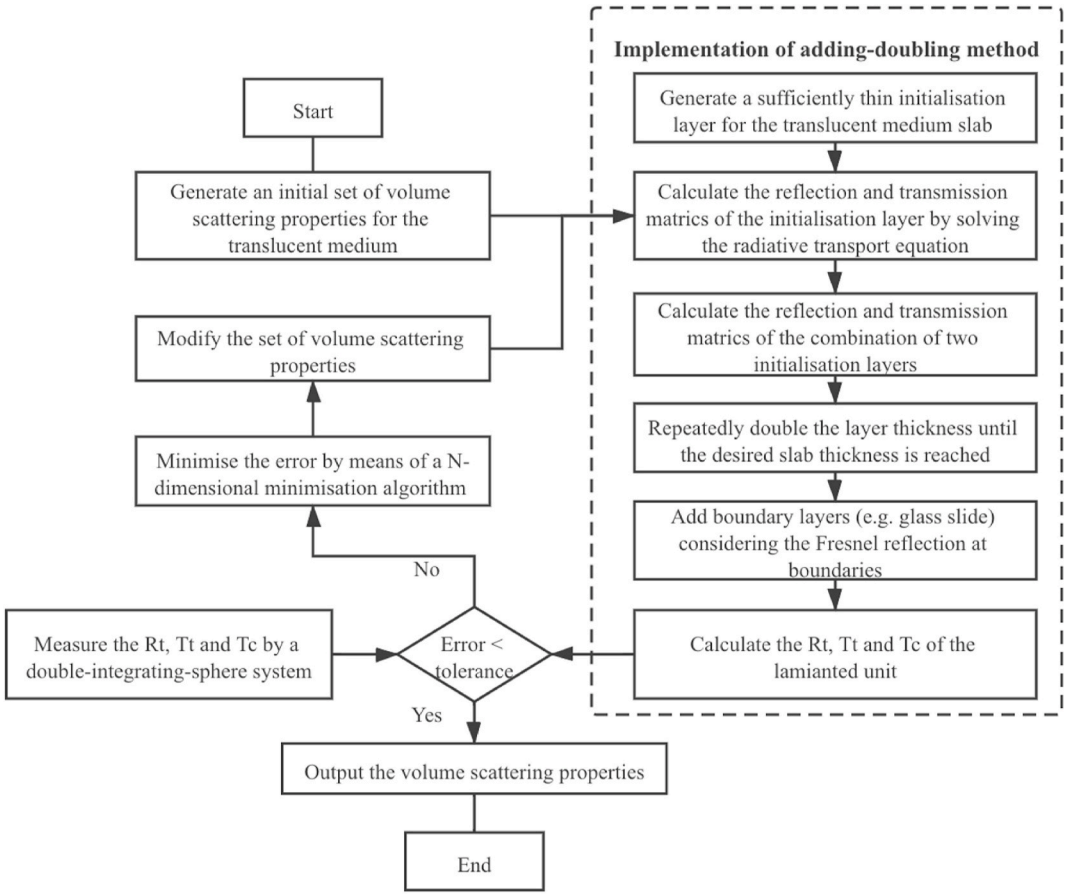

Fig. 6. Inverse adding-doubling algorithm for determining the volume scattering properties of a translucent medium.

$$\mu_s = \frac{\mu_s'}{(1-g)} \tag{1}$$

$$p(\theta) = \frac{1}{4\pi} \frac{1-g^2}{(1+g^2-2g\cos(\theta))^{3/2}} \tag{2}$$

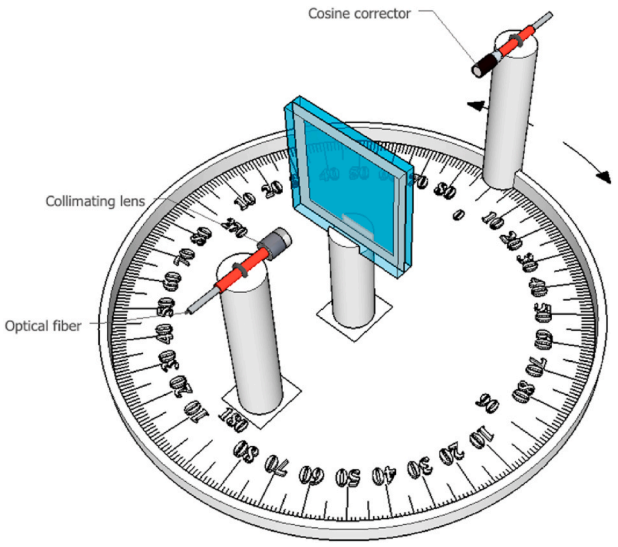

Fig. 7. Schematic diagram of the angular intensity measurement setup.

Ocean Optics LS-1-CA calibrated halogen lamp. The intensities of light transmitted through the sample observed at the angles of 0°, 15°, 30°, 45° and 60° were measured and compared to the simulation results using the developed optical model. After validation, the normalised scattered radiant intensity of the thermotropic laminated glazing sample as a function of scattering angle was calculated, given by Eq.(3) [37].

$$F(\theta) = \frac{G_s(\theta)}{G_i \times \Omega} = \frac{G_s(\theta)}{G_i \times \frac{A}{R^2}} \tag{3}$$

Where $F(\theta)$ is the normalised angular scattering intensity, $G_s(\theta)$ is the scattering intensity of the sample detected at the scattering angle θ (W/m^2), G_i is the normal incident light intensity (W/m^2), Ω is the solid angle of the detector, A is the surface area of the detector port (m^2), and R is the distance between the detector port and the centre of the sample (m).

3. Results and discussion

3.1. Total transmittance, total reflectance and collimated transmittance

Fig. 8 shows the total transmittance and total reflectance of the sample consisting of a 1-mm-thick 2 wt% HPC, 1.5 wt% GGF based thermotropic membrane sandwiched by two pieces of 4-mm-thick optical glass panes, measured over the membrane temperature range from

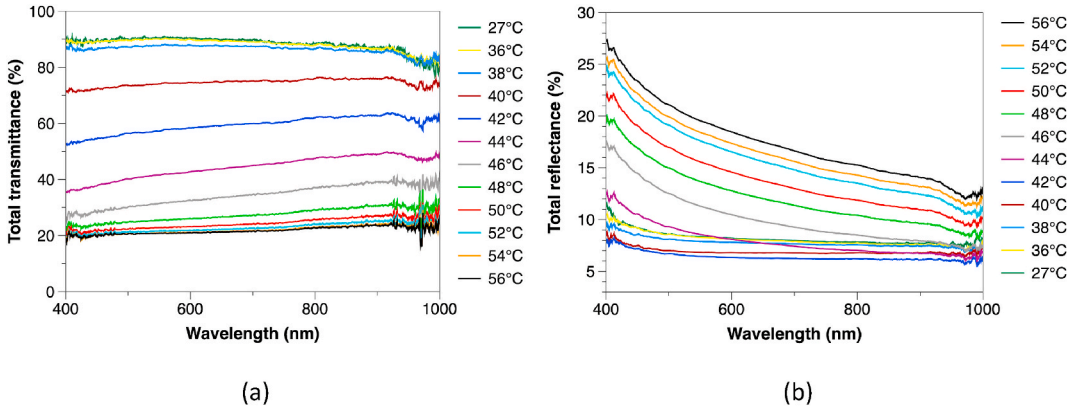

Fig. 8. (a) Spectral total transmittance and (b) spectral total reflectance of a laminated glazing sample with a 2 wt% HPC, 1.5 wt% GGF based TT membrane under various temperature conditions.

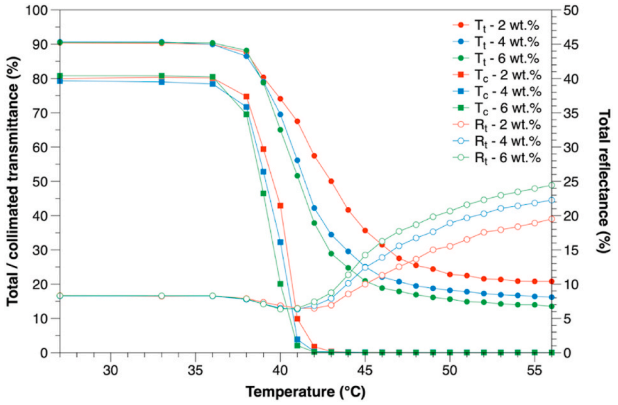

Fig. 9. Average visible total transmittance, total reflectance and collimated transmittance of the three laminated glazing samples with the TT membranes consisting of 2, 4 and 6 wt% HPC with 1.5 wt% GGF, as a function of membrane temperature.

27 to 56 °C and the wavelength range from 400 to 1000 nm. As shown in Fig. 8(a), the total transmittance of the sample decreases with increasing temperature, being approximately 90% at temperatures below 38 °C and nearly 20% above 50 °C. This is because HPC is freely soluble in the water below 38°C, whereas is insoluble and precipitates as white floc in water above 38°C, resulting in a translucent appearance [35,38,39], as can also be seen in Fig. 5. The transition temperature of the 2 wt% HPC membrane (i.e. quoted as the temperature at which 50% of incoming solar radiation transmits through the sample [31]) is approximately 42°C.

On the other hand, the total reflectance is below 10% at 27°C, decreases slightly when the temperature increases from 38 to 42°C, and then increases progressively with temperature, as shown in Fig. 8(b). A similar phenomenon was reported by Varma et al. [40]. This might be due to the combined effect of specular reflection decrease and diffuse reflection increase. The specular reflection decrease might be attributed to an increase in the refractive index of the thermotropic hydrogel, induced by its volumetric change with temperature [41]. A possible reason for the diffuse reflection increase may be that the number and size of HPC aggregates (i.e. scattering centres) in the membrane structure increase due to continuous phase separation [42].

Fig. 9 shows the average values of total transmittance (T_t), collimated transmittance (T_c) and total reflectance (R_t) in the visible region (380–780 nm) (calculated following the methods outlined in the BSI Standard BS EN 410:2011 [43]) for the laminated glazing samples with the 2, 4 and 6 wt% HPC membranes under various temperature conditions. The samples exhibit similar total transmittances (~90%), collimated transmittances (~80%) and total reflectances (~8%) when below 38°C. The differences between the total and collimated transmittances imply that the light passing through the samples in the transparent state is not entirely in the specular direction. A fraction of light incident on the samples is diffused, probably because of unsmooth surfaces and impurities. As can be seen from Fig. 9, the total and collimated transmittances both start to decrease at 38°C. However, the collimated transmittance decreases faster than the total transmittance, indicating an increase in the proportion of diffusely to totally transmitted light through the sample. When the membrane temperature increases to 42°C, the collimated transmittances of the three samples are nearly 0% whereas their total transmittances are higher than 35%. The transmittance differences suggest that the thermotropic membranes potentially can be used in windows to reduce glare caused by direct lighting. As the membrane temperature reaches 56°C, the total transmittances of the samples with 2, 4 and 6 wt% HPC decrease to ~ 21%, ~16% and ~14%, respectively. The total reflectances of the samples increase with temperature when the samples are heated above 42°C. A higher HPC concentration results in higher total reflectance but lower total and collimated transmittances in the phase separation process. This could be attributed to an increased amount of HPC aggregates within the membrane structure, increasing the opportunity for light to be scattered.

3.2. Volume scattering properties

Based on the measured spectral transmittance and reflectance, the spectral volume scattering properties of the thermotropic membrane were calculated with the IAD method. Fig. 10 shows the effect of membrane temperature on the volume scattering properties of the thermotropic membrane consisting of 2 wt% HPC and 1.5 wt% GGF over the wavelength range from 400 to 1000 nm. It can be seen that the reduced scattering coefficient (μ_s') increases when the membrane temperature increases from 44 to 56 °C. This trend corroborates that the thermotropic membrane becomes increasingly diffusely reflective and transmissive in the heating process as aforementioned. On the other hand, the temperature effect on the sample's absorption coefficient (μ_a) is as not significant as on the μ_s'. The anisotropy factor (g) is observed to decrease with increasing temperature, indicating an increasing proportion of light being scattered backwards from the thermotropic membrane.

Fig. 11 shows the volume scattering properties calculated for the 2, 4 and 6 wt% HPC based thermotropic membranes at the wavelength of 600 nm. As can be seen from Fig. 11, the three membranes exhibit similar temperature dependences of the volume scattering properties. Taking the 6 wt% HPC as an example, when the membrane temperature increases from 44 to 56 °C, the μ_s' increases from 0.78 to 2.41 mm^{-1}, the μ_a reduces from 0.55 to 0.42 mm^{-1}, and the g reduces from 0.88 to 0.67.

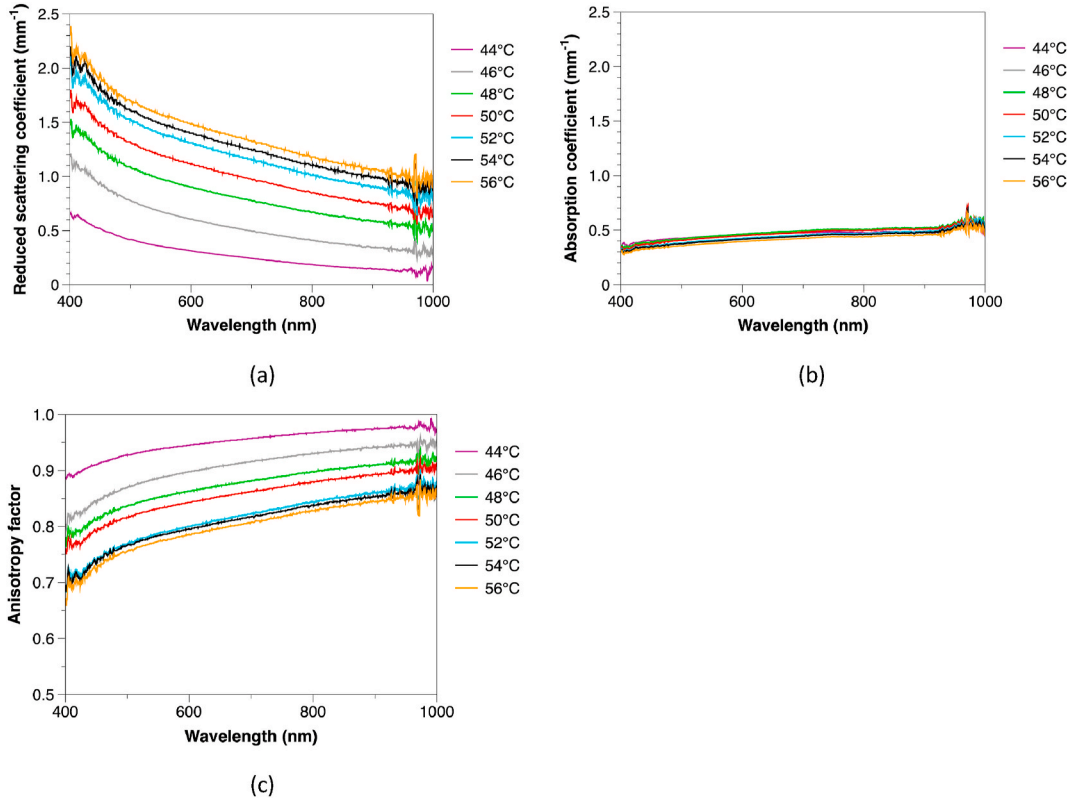

Fig. 10. (a) Reduced scattering coefficient, (b) absorption coefficient and (c) anisotropy factor of the 2 wt% HPC, 1.5 wt% GGF based TT membrane under various temperatures.

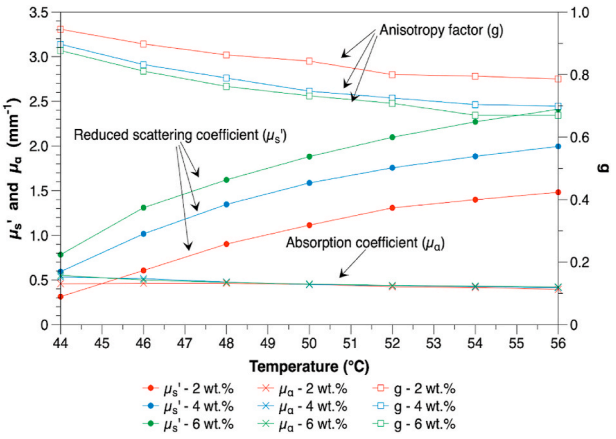

Fig. 11. Volume scattering properties of the 2, 4 and 6 wt% HPC based TT membranes at the wavelength of 600 nm as a function of membrane temperature.

It is also found that at the same temperatures, the membranes with greater HPC concentrations have higher μ_s' but lower g. For example, at 56 °C, the μ_s' increases from 1.48 to 2.41 mm^{-1}, while the g decreases from 0.79 to 0.67, with increasing the HPC concentration from 2 to 6 wt %. Similar trends regarding the effects of temperature and HPC concentration are observed at the wavelengths of 400 nm and 800 nm, as can be seen in Table 1.

The effect of the wavelength of incident light on the volume scattering properties of the thermotropic membranes has also been investigated. As can be seen from Table 1 and Fig. 10, the μ_s' is lower and the g is higher at a longer wavelength. This might be because the radiative scattering behaviour of a translucent material is related to the particle size parameter ($x = 2\pi a/\lambda$), which is determined by the wavelength of incident light (λ) and the particle radius (a) [44,45]. The longer the wavelength, the smaller the value of x, therefore the less effectively light is scattered by the particles, and also the larger the angle between the incident and scattered directions [44,45].

3.3. Angular scattering profile and spatial flux distribution

The volume scattering properties determined in the previous section were used as input data to the Monte-Carlo ray-tracing model, where an irradiance detector rotates around the thermotropic laminated glazing sample to collect the scattered light at a specific angle from the sample (Fig. 7). Fig. 12 shows the results of detected irradiance from the optical simulation (circle points) and the measurement (cross points). Good agreement is obtained between the simulated and measured results for the selected scattering angles (0°, 15°, 30°, 45° and 60°), membrane temperatures (48, 50 and 52°C) and HPC concentrations (2, 4 and 6 wt %). The validated results give confidence in the use of the optical modelling approach to predict the angular scattering profile and spatial flux distribution of the thermotropic membranes under different conditions.

The validated optical model has been subsequently used to investigate the angular scattering intensity distribution of the thermotropic laminated glazing sample when subjected to the changes in membrane temperature and HPC concentration. As can be seen from Fig. 13(a), the 2 wt% HPC based sample at 44 °C exhibits narrow-angle forward scattering, i.e. most of the incident light is scattered forwards within the angle range from 345° to 15°. The forward-scattering peak reduces significantly with the membrane temperature increasing from 44 to 56 °C, as shown in Fig. 13(a) and (b). For instance, the normalised radiant intensity at the scattering angle of 0° reduces from ~1 sr^{-1} to ~0.18 sr^{-1} when the membrane temperature increases from 44 to 48 °C, and further to ~0.09 sr^{-1} when above 54 °C. On the other hand, the

Table 1
Volume scattering properties with respect to different HPC concentrations, membrane temperatures and wavelengths.

		400 nm				600 nm				800 nm			
		μ_s'	μ_s	μ_a	g	μ_s'	μ_s	μ_a	g	μ_s'	μ_s	μ_a	g
Unit	°C	mm^{-1}	mm^{-1}	mm^{-1}	/	mm^{-1}	mm^{-1}	mm^{-1}	/	mm^{-1}	mm^{-1}	mm^{-1}	/
2 wt%	44	0.67	5.81	0.36	0.88	0.31	5.70	0.46	0.95	0.19	5.69	0.48	0.97
	50	1.72	7.22	0.33	0.76	1.11	7.10	0.45	0.84	0.85	7.05	0.49	0.88
	56	2.30	7.01	0.29	0.67	1.48	6.91	0.40	0.79	1.18	6.87	0.44	0.83
4 wt%	44	1.06	5.88	0.43	0.82	0.59	5.77	0.53	0.90	0.42	5.73	0.57	0.93
	50	2.53	6.35	0.36	0.60	1.59	6.26	0.45	0.75	1.27	6.21	0.50	0.80
	56	2.99	6.71	0.33	0.55	2.00	6.63	0.41	0.70	1.63	6.59	0.45	0.75
6 wt%	44	1.28	6.45	0.44	0.80	0.78	6.34	0.55	0.88	0.58	6.30	0.60	0.91
	50	2.86	7.11	0.35	0.60	1.88	7.01	0.45	0.73	1.51	6.96	0.50	0.78
	56	3.63	7.37	0.35	0.51	2.41	7.30	0.42	0.67	1.99	7.26	0.46	0.73

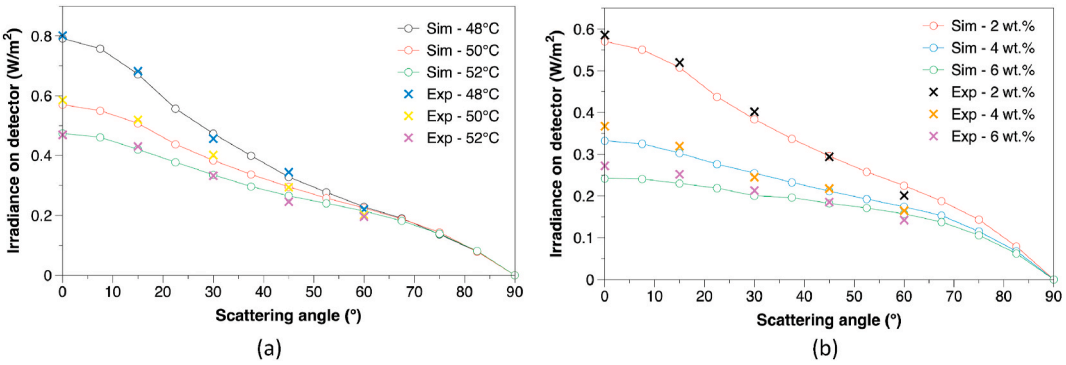

Fig. 12. Comparison between the simulated and measured irradiances for (a) the sample with 2 wt% HPC at 48, 50 and 52 °C, and (b) the samples with 2, 4 and 6 wt % HPC at 50 °C.

backward scattering becomes more prominent at higher membrane temperatures. In addition to the temperature effect, the angular scattering intensity distribution shows dependence on the HPC concentration. Fig. 13(c) and (d) illustrate that increasing the HPC concentration from 2 to 6 wt% results in suppressed forward scattering and enhanced backward scattering at the membrane temperatures of 50 and 56 °C. Similar trends are observed for the other membrane temperatures in the range from 44 to 56 °C (results not shown here). The results from Fig. 13 (c) and (d) also show that increasing the HPC concentration results in a more uniform angular intensity distribution of the light scattered in the forward direction, which can potentially reduce the intensity contrast between the glare area and its neighbouring area thus providing more effective glare protection for buildings.

Fig. 14 illustrates the spatial flux distributions when light propagates in the 2 wt% and 6 wt% HPC based thermotropic layers at the three membrane temperatures: 44, 50 and 56 °C. A light beam with a diameter of 0.5 mm was assumed to perpendicularly enter the top surface of the 1-mm-thick thermotropic layer (i.e. Y = 0). All the other settings are the same as in the previous optical simulations. As shown in Fig. 14, the incident flux in the X range from −0.25 to 0.25 mm decreases with the depth increasing. The light attenuation is caused by the absorption and scattering in the thermotropic membrane. Due to the volume scattering, the light beam spreads in the transverse direction during propagation in the thermotropic layer. When the membrane temperature increases from 44 to 56 °C or the HPC concentration increases from 2 to 6 wt%, the flux reaching the bottom surface (i.e. Y = −1) decreases, which results in reductions in the total transmittance (Fig. 9) and forward scattering peak (Fig. 13) of the thermotropic laminated glazing sample.

3.4. Optical design and characterisation of BIPV smart window

The developed optical model has been used to predict the effects of various parameters (e.g. HPC concentration, membrane thickness, geometric concentration ratio and glass refractive index) on the performance of the proposed BIPV smart window. Subsequently, a prototype for the BIPV smart window and a prototype for the counterpart PV window of similar structure but with no HPC membrane (named reference system) have been fabricated based on the findings from the optical simulation. A schematic diagram for the BIPV smart window for initial optical modelling is illustrated in Fig. 15. The BIPV smart window has a four-layer structure: a Dow Corning 1–2577 optical coating layer for encapsulating the solar cell (10 mm × 10 mm), a thermotropic membrane layer (50 mm × 50 mm × 1 mm) for modulating incident solar radiation and two GPE Scientific low-iron glass covers (50 mm × 50 mm × 4 mm). The thermotropic membrane layer was modelled using the sets of volume scattering properties (μ_a, μ_s and g) corresponding to the membrane temperatures from 44 to 56°C. The average refractive indices of the glass covers and the optical coating layer were defined as 1.51 and 1.49, respectively. The solar cell was assumed as a perfect light absorber (i.e. 100% absorptivity) for simplicity. AM1.5G sunlight with the power density of 1000 W/m^2 [46] perpendicularly illyilluminated on the front glazing cover of the BIPV smart window. The ray number was set as 1, 000,000 conformed by a ray independence study.

The effects of membrane temperature and HPC concentration on the optical performance of the BIPV smart window have been investigated and are shown in Fig. 16(a). When the membrane temperature increases from 44 to 56°C, the optical power density (i.e. irradiance at the solar cell surface) of the BIPV smart window with the 2 wt% HPC membrane increases from 958 to 1028 W/m^2, higher than that of the reference system (930 W/m^2). This is because the thermotropic membrane offers stronger backward scattering at higher temperatures (see Fig. 13), resulting in an increased fraction of incident light being reflected and redirected through Total Internal Reflection (TIR) towards the solar cell. Fig. 16(a) also shows that higher optical power densities can be achieved by increasing the HPC concentration, for example, the optical power densities at 56°C for the 2, 4 and 6 wt% HPC concentrations are 1028,

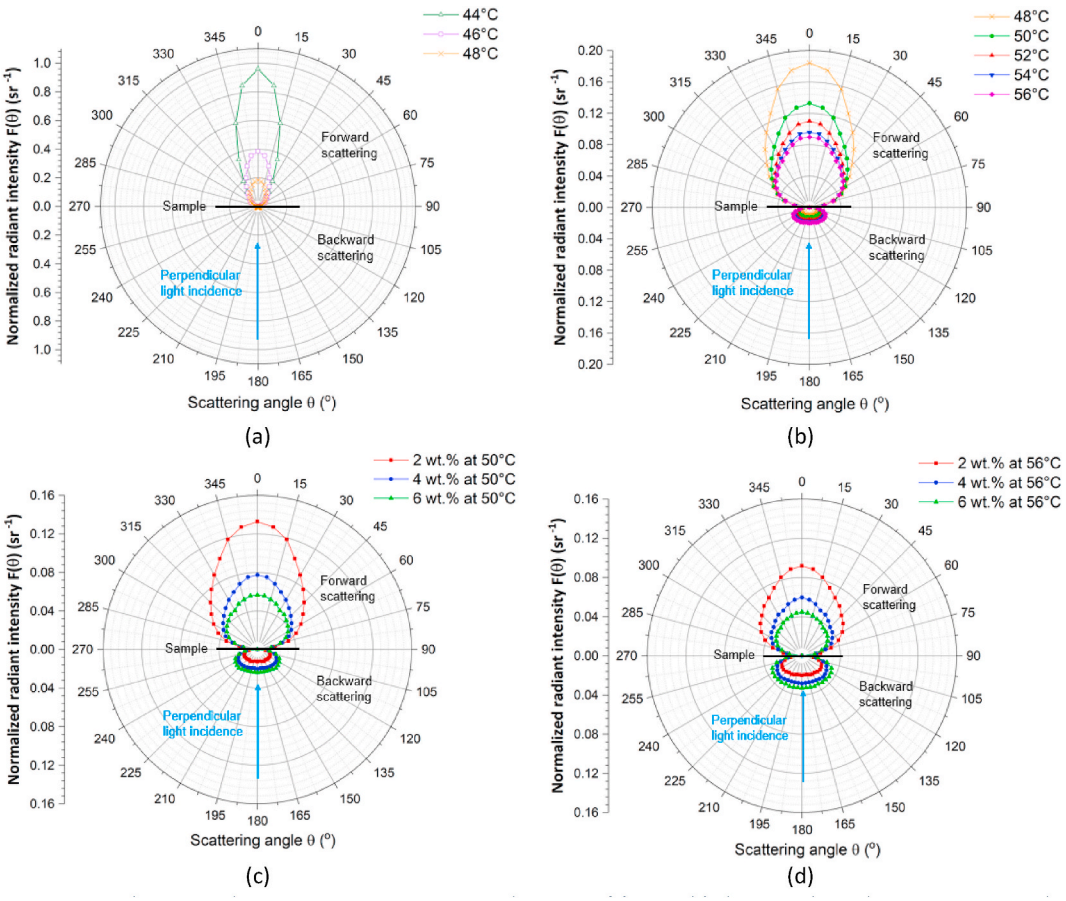

Fig. 13. Normalised angular scattering intensity distributions of (a and b) the sample with 2 wt% HPC at the membrane temperatures from 44 to 56 °C, (c and d) the samples with 2, 4 and 6 wt% HPC at the membrane temperatures of 50 °C and 56 °C.

1047 and 1061 W/m^2, respectively. Therefore, the HPC concentration of 6 wt% was selected for further parametric studies.

The optical performance of the BIPV smart window with a 6 wt% HPC membrane at different thicknesses is illustrated in Fig. 16(b). The optical power density increases significantly with the membrane thickness increasing from 0.1 to 0.5 mm. A possible reason may be that using a thicker membrane increases the number of scattering events along the path of propagation, thus causing more photons to be scattered to the solar cell. With further increasing the membrane thickness above 1 mm, it is observed that there is no significant increase in optical power density, probably because the contribution of longer path length travelled photons to the light reflectance is less significant [47]. In other words, the reflected solar energy is mainly contributed by the near-surface volume scattering [11].

Fig. 16(c) illustrates the relationship between the geometric concentration ratio (i.e. the ratio between the aperture areas of the front glazing cover and solar cell) and the optical performance of the BIPV smart window with a 1-mm-thick 6 wt% HPC membrane. Taking the membrane temperature of 56°C as an example, when the geometric concentration ratio is increased from 4 to 16, the optical power density increases from 1019 to 1057 W/m^2. This is due to a larger area of the thermotropic membrane available, resulting in more photons being reflected and concentrated on the solar cell. There is a slight increase to 1064 W/m^2 when the geometric concentration ratio is further raised to 32, indicating that most of the photons scattered from the expansion area could not be collected by the solar cell. The optical losses could be potentially attributed to the escaping of photons from the window system and the absorption of photons in the coating/glass/membrane before reaching the solar cell.

The refractive index of the front glazing cover is another factor affecting the optical performance of the BIPV smart window. As can be seen from Fig. 16(d), the curve of optical power density plotted against membrane temperature shifts downwards as the refractive index is increased from 1.52 to 1.71. This may be because the front glazing cover with a higher refractive index has lower optical transmittance and reduces the direct sunlight received by the solar cell.

After considering all the factors affecting the BIPV smart window performance, the HPC concentration of 6 wt% with the membrane thickness of 1 mm, the geometric concentration ratio of 16 and the glass refractive index of 1.52 was selected and applied for the prototype development.

3.5. Experimental investigation

The optimised prototype of the BIPV smart window has been characterised by an indoor environmental experiment. The electrical performance of the prototype illuminated under a tungsten halogen lamp was measured using a Keithley 2420 source meter unit. The incident light intensity and the ambient air temperature were controlled to be 90 mW/cm^2 and 25°C respectively. Fig. 17(a) shows the current-voltage (I–V) characteristics at different membrane temperatures of the prototype BIPV smart window. The short-circuit current density increases by 17.8% from 27.8 to 32.8 mA/cm^2 with the membrane temperature increasing from 42 to 54°C, and meanwhile, the maximum power output increases by 12.1%. The result demonstrates that the BIPV smart window system can produce more electricity when the integrated thermotropic membrane provides stronger light scattering while subjected to higher temperatures above its transition temperature.

Based on the experimental results, the ratio of short-circuit currents generated from the prototype BIPV smart window ($I_{sc,\ BICPV}$) and from its

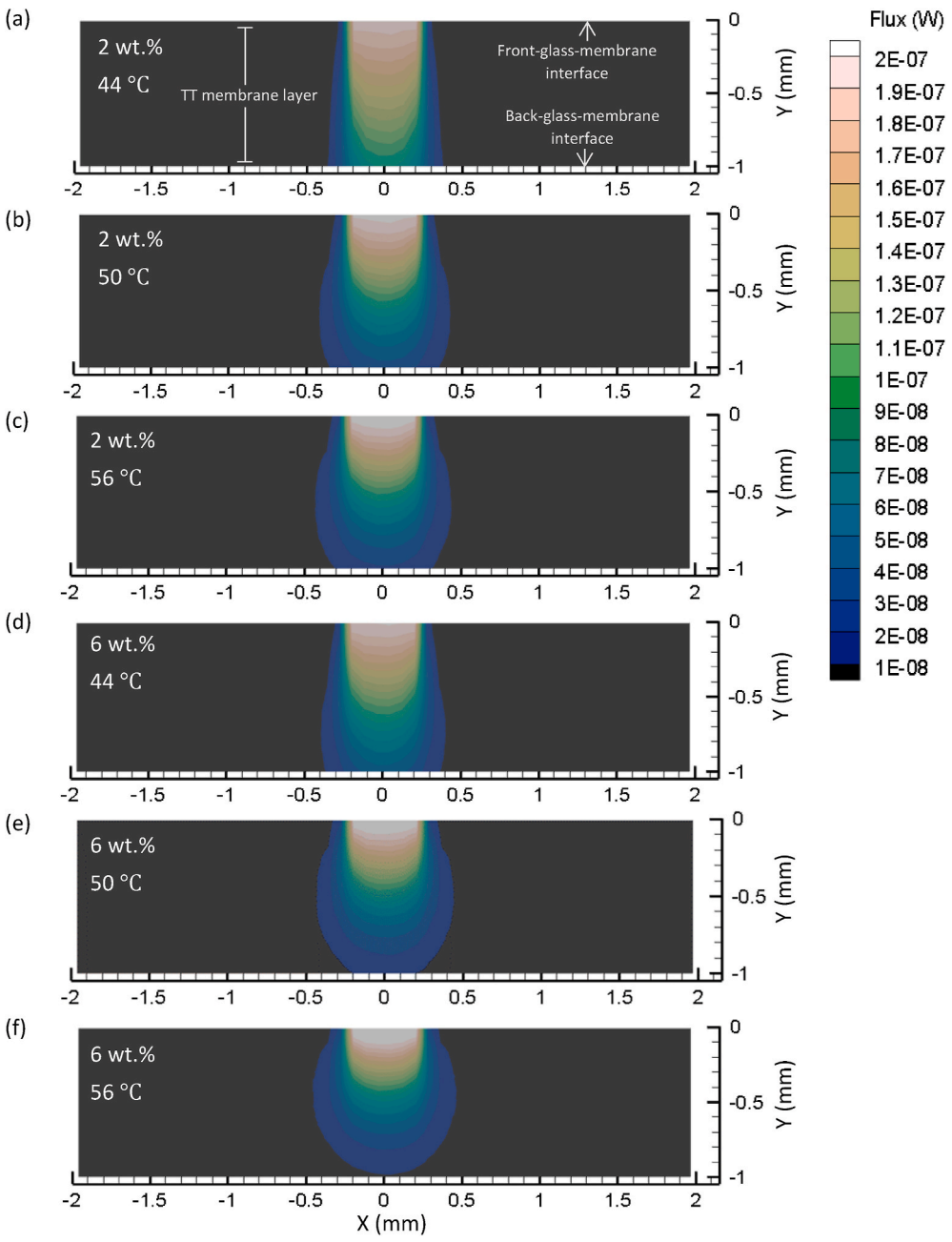

Fig. 14. Cross-section views of the incident flux distribution in the TT membrane layer with 1 mm thickness for (a–c) 2 wt% HPC and (d–f) 6 wt% HPC at 44, 50 and 56 °C, respectively.

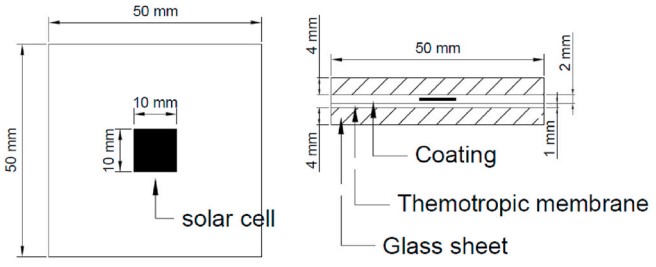

Fig. 15. Configuration of the BIPV smart window prototype for optical analysis.

counterpart system with no membrane (reference system) ($I_{sc,\ ref}$) was calculated. From Fig. 17(b), it can be seen that the short-circuit current ratio increases from 1.053 to 1.145, with the membrane temperature increasing from 44 to 56 °C. Since the short-circuit current produced by a solar cell can be taken as directly proportional to the irradiance at the cell surface [7,48,49], the ratio of irradiances between the prototype BIPV smart window ($G_{s,\ BIPV}$) and the reference system ($G_{s,\ ref}$) can be expressed by Eq.(4). The irradiance ratios at various membrane temperatures derived from the experiment and optical simulation are presented in Table 2. The simulation results give good agreement with the experimental results, with differences of less than 1%. This validation confirms the usefulness of the optical modelling approach for predicting the dynamic behaviours of the BIPV smart window system.

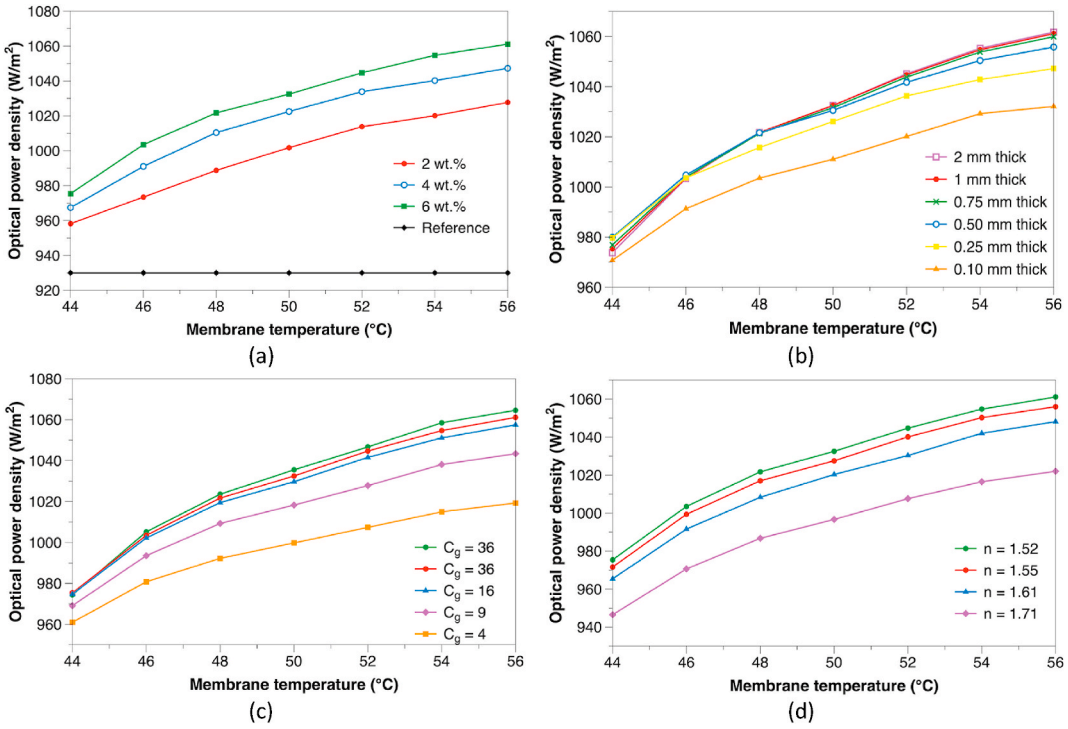

Fig. 16. Optical power density for the BIPV smart windows based on (a) different HPC concentrations, membrane thickness d = 1 mm, geometric concentration ratio $C_g = 25$ and refractive index of the front glass cover n = 1.52; (b) 6 wt% HPC, different thicknesses, $C_g = 25$ and n = 1.52; (c) 6 wt% HPC, d = 1 mm, different C_g and n = 1.52; (d) 6 wt% HPC, d = 1 mm, $C_g = 25$ and different refractive indices.

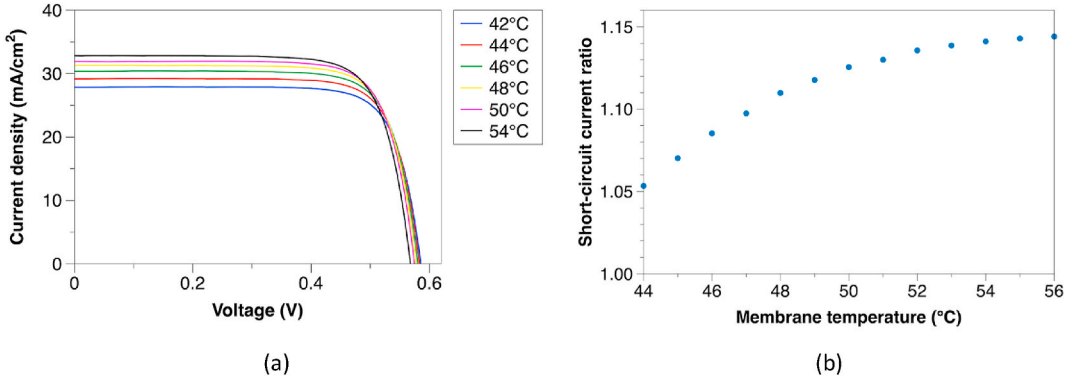

Fig. 17. (a) I–V characteristics of the BIPV smart window prototype at different membrane temperatures. (b) The ratio of short-circuit currents between the BIPV smart window and the reference system as a function of membrane temperature.

$$\frac{I_{sc,\,BIPV}}{I_{sc,\,ref}} = \frac{G_{s,\,BIPV}}{G_{s,\,ref}} \tag{4}$$

Table 2
Experimental and simulated irradiance ratios at different membrane temperatures.

		44 °C	46 °C	48 °C	50 °C	52 °C	54 °C	56 °C
$G_{s,BIPV}$ / $G_{s,\,ref}$	Experiment	1.053	1.085	1.109	1.125	1.135	1.141	1.145
	Simulation	1.050	1.080	1.101	1.116	1.127	1.136	1.143
	Difference	0.3%	0.5%	0.7%	0.8%	0.7%	0.4%	0.2%

4. Conclusions

This study developed an advanced optical model for the design and characterisation of a Building Integrated (BIPV) smart window system with a thermotropic hydrogel membrane applied. To be more specific, a numerical method based on Inverse Adding-Doubling (IAD) calculation coupled with Double-Integrating-Sphere (DIS) spectroscopic measurements has been firstly used to determine the volume scattering properties of Hydroxypropyl Cellulose (HPC) based thermotropic hydrogel membranes. Subsequently, a Monte-Carlo ray-tracing model using the

volume scattering properties obtained from the IAD has been developed to predict the dynamic behaviours of the developed thermotropic membranes (2, 4 and 6 wt% HPC) and optimise the design of the proposed BIPV smart window system. The simulation predictions were found to be in good agreement with the experimental results. The key findings and conclusions are as follows:

1) The total transmittance of the thermotropic laminated glazing sample (2 wt% HPC) reduces from ~90% to ~20% and the collimated transmittance reduces from ~80% to ~0%, with the membrane temperature increasing from 27 to 56°C. These features indicate that the developed thermotropic membrane offers good potential for application in windows to avoid excessive solar heating and glare.
2) The optical simulation results show that increasing membrane temperature or HPC concentration leads to stronger backward scattering from the thermotropic membrane, resulting in an improved power output of the BIPV smart window.
3) There is no significant improvement in power generation when the geometric concentration ratio of the BIPV smart window (6 wt% HPC) exceeds 16× and the membrane thickness is greater than 1 mm.
4) The optimised prototype of the BIPV smart window shows an increase in short-circuit current density by 17.8% and an increase in maximum power output by 12.1% with the membrane temperature increasing from 42 to 54°C.
5) The short-circuit current of the prototype BIPV smart window is up to 1.15 times higher than that of its counterpart system of similar structure but with no membrane.

This paper presents a generalised method for evaluating the scattering characteristics of translucent media (e.g. thermotropic hydrogels) and demonstrates the feasibility of the proposed BIPV smart window system for electricity generation and adaptive daylighting control.

CRediT authorship contribution statement

Xiao Liu: Methodology, Project administration, Investigation, Data curation, Writing - original draft. **Yupeng Wu:** Resources, Funding acquisition, Supervision, Methodology, Writing - review & editing.

Declaration of competing interest

The authors declare that they have no known competing financial interests or personal relationships that could have appeared to influence the work reported in this paper.

Acknowledgement

This work was supported by the Faculty of Engineering, University of Nottingham and the China Scholarship Council through a joint PhD studentship awarded to Xiao Liu. This work was also supported by the Engineering and Physical Sciences Research Council, UK [grant number EP/S030786/1].

References

[1] B. Norton, P.C. Eames, T.K. Mallick, M.J. Huang, S.J. McCormack, J.D. Mondol, Y. G. Yohanis, Enhancing the performance of building integrated photovoltaics, Sol. Energy 85 (8) (2011) 1629–1664.
[2] N. Skandalos, D. Karamanis, PV glazing technologies, Renew. Sustain. Energy Rev. 49 (2015) 306–322.
[3] A. Ghosh, Potential of building integrated and attached/applied photovoltaic (BIPV/BAPV) for adaptive less energy-hungry building's skin: a comprehensive Review, J. Clean. Prod. (2020) 123343.
[4] H. Baig, N. Sarmah, K.C. Heasman, T.K. Mallick, Numerical modelling and experimental validation of a low concentrating photovoltaic system, Sol. Energy Mater. Sol. Cell. 113 (2013) 201–219.
[5] H. Baig, N. Sellami, T.K. Mallick, Performance modeling and testing of a building integrated concentrating photovoltaic (BICPV) system, Sol. Energy Mater. Sol. Cell. 134 (2015) 29–44.
[6] A. Kerrouche, D. Hardy, D. Ross, B. Richards, Luminescent solar concentrators: from experimental validation of 3D ray-tracing simulations to coloured stained-glass windows for BIPV, Sol. Energy Mater. Sol. Cell. 122 (2014) 99–106.
[7] N. Sellami, T.K. Mallick, Optical characterisation and optimisation of a static window integrated concentrating photovoltaic system, Sol. Energy 91 (2013) 273–282.
[8] K. Shanks, A. Knowles, A. Brierley, H. Baig, H. Orr, Y. Sun, Y. Wu, S. Sundaram, T. Mallick, An experimental analysis of the optical, thermal and power to weight performance of plastic and glass optics with AR coatings for embedded CPV windows, Sol. Energy Mater. Sol. Cell. 200 (2019) 110027.
[9] J.M. Kim, P.S. Dutta, Optical efficiency–concentration ratio trade-off for a flat panel photovoltaic system with diffuser type concentrator, Sol. Energy Mater. Sol. Cell. 103 (2012) 35–40.
[10] Y. Wu, K. Connelly, Y. Liu, X. Gu, Y. Gao, G.Z. Chen, Smart solar concentrators for building integrated photovoltaic façades, Sol. Energy 133 (2016) 111–118.
[11] M. Neuman, P. Edström, Anisotropic reflectance from turbid media, *I. Theory*. JOSA A 27 (5) (2010) 1032–1039.
[12] M.R. Shenoy, B.P. Pal, Method to determine the optical properties of turbid media, Appl. Optic. 47 (17) (2008) 3216–3220.
[13] A. Correia, P. Hanselaer, H. Cornelissen, Y. Meuret, Radiance based method for accurate determination of volume scattering parameters using GPU-accelerated Monte Carlo, Optic Express 25 (19) (2017) 22575–22586.
[14] D. Hu, R. Lu, Y. Huang, Y. Ying, X. Fu, Effects of optical variables in a single integrating sphere system on estimation of scattering properties of turbid media, Biosyst. Eng. 194 (2020) 82–98.
[15] J.W. Pickering, S.A. Prahl, N. Van Wieringen, J.F. Beek, H.J. Sterenborg, M.J. Van Gemert, Double-integrating-sphere system for measuring the optical properties of tissue, Appl. Optic. 32 (4) (1993) 399–410.
[16] S.A. Prahl, M.J. van Gemert, A.J. Welch, Determining the optical properties of turbid media by using the adding–doubling method, Appl. Optic. 32 (4) (1993) 559–568.
[17] A. Córreia, H. Cornelissen, S. Leyre, P. Hanselaer, Y. Meuret, Determination of volume scattering parameters that reproduce the luminance characteristics of diffusers, Optic Express 24 (11) (2016) 11727–11738.
[18] A. Correia, P. Hanselaer, Y. Meuret, Accurate and robust characterization of volume scattering materials using the intensity-based inverse adding-doubling method. Modeling Aspects in Optical Metrology VII, International Society for Optics and Photonics, 2019.
[19] S. Leyre, F.B. Leloup, J. Audenaert, G. Durinck, J. Hofkens, G. Deconinck, P. Hanselaer, Determination of the bulk scattering parameters of diffusing materials, Appl. Optic. 52 (18) (2013) 4083–4090.
[20] D.K. Sardar, B.G. Yust, F.J. Barrera, L.C. Mimun, A.T. Tsin, Optical absorption and scattering of bovine cornea, lens and retina in the visible region, Laser Med. Sci. 24 (6) (2009) 839–847.
[21] H. Cen, R. Lu, Optimization of the hyperspectral imaging-based spatially-resolved system for measuring the optical properties of biological materials, Optic Express 18 (16) (2010) 17412–17432.
[22] S. Bellini, R. Bendoula, E. Latrille, J.-M. Roger, Potential of a spectroscopic measurement method using adding-doubling to retrieve the bulk optical properties of dense microalgal media, Appl. Spectrosc. 68 (10) (2014) 1154–1167.
[23] H. Assadi, R. Karshafian, A. Douplik, Optical scattering properties of intralipid phantom in presence of encapsulated microbubbles, Int. J. Photoenergy 2014 (2014), 471764, https://doi.org/10.1155/2014/471764.
[24] S. Prahl, Everything I Think You Should Know about Inverse Adding-Doubling, Oregon Medical Laser Center, St. Vincent Hospital, 2011, pp. 1–74.
[25] P.I. Rowe, R. Künnemeyer, A. McGlone, S. Talele, P. Martinsen, R. Seelye, Relationship between tissue firmness and optical properties of 'Royal Gala' apples from 400 to 1050 nm, Postharvest Biol. Technol. 94 (2014) 89–96.
[26] W. Wang, C. Li, Measurement of the light absorption and scattering properties of onion skin and flesh at 633 nm, Postharvest Biol. Technol. 86 (2013) 494–501.
[27] A. Ionescu, J. Cardona, I. Garzón, A. Oliveira, R. Ghinea, M. Alaminos, M. Pérez, Integrating-sphere measurements for determining optical properties of tissue-engineered oral mucosa, Journal of the European Optical Society-Rapid publications 10 (2015).
[28] M.S. Wróbel, A.P. Popov, A.V. Bykov, V.V. Tuchin, M. Jędrzejewska-Szczerska, Nanoparticle-free tissue-mimicking phantoms with intrinsic scattering, Biomed. Optic Express 7 (6) (2016) 2088–2094.
[29] S. Leyre, Y. Meuret, G. Durinck, J. Hofkens, G. Deconinck, P. Hanselaer, Estimation of the effective phase function of bulk diffusing materials with the inverse adding-doubling method, Appl. Optic. 53 (10) (2014) 2117–2125.
[30] B. Xie, Y. Cheng, J. Hao, W. Shu, K. Wang, X. Luo, Precise optical modeling of quantum dots for white light-emitting diodes, Sci. Rep. 7 (1) (2017) 1–10.
[31] K. Connelly, Y. Wu, J. Chen, Y. Lei, Design and development of a reflective membrane for a novel building integrated concentrating photovoltaic (BICPV) 'smart window' system, Appl. Energy 182 (2016) 331–339.
[32] S.A. Prahl, M.J.C. van Gemert, A.J. Welch, Determining the optical properties of turbid media by using the adding–doubling method, Appl. Optic. 32 (4) (1993) 559–568.
[33] S.A. Prahl, The adding-doubling method. Optical-thermal Response of Laser-Irradiated Tissue, Springer, 1995, pp. 101–129.
[34] M.S. Wróbel, A.P. Popov, A.V. Bykov, M. Kinnunen, M. Jędrzejewska-Szczerska, V. V. Tuchin, Measurements of fundamental properties of homogeneous tissue phantoms, J. Biomed. Optic. 20 (4) (2015), 045004.

[35] R.C. Rowe, P. Sheskey, M. Quinn, Handbook of Pharmaceutical Excipients, Libros Digitales-Pharmaceutical Press, 2009.
[36] T. Wüstenberg, Cellulose and Cellulose Derivatives in the Food Industry: Fundamentals and Applications, John Wiley & Sons, 2014.
[37] J. Wang, C. Xu, A.M. Nilsson, D.L. Fernandes, M. Strömberg, J. Wang, G. A. Niklasson, General method for determining light scattering and absorption of nanoparticle composites, Adv Optic Mater 7 (4) (2019) 1801315.
[38] S. Fortin, G. Charlet, Phase diagram of aqueous solutions of (hydroxypropyl) cellulose, Macromolecules 22 (5) (1989) 2286–2292.
[39] K. Connelly, Y. Wu, X. Ma, Y. Lei, Transmittance and reflectance studies of thermotropic material for a novel building integrated concentrating photovoltaic (BICPV)'Smart Window'System, Energies 10 (11) (2017) 1889.
[40] S. Varma, L. Bureau, D. Débarre, The conformation of thermoresponsive polymer brushes probed by optical reflectivity, Langmuir 32 (13) (2016) 3152–3163.
[41] Q. Wang, L. Liu, Y. Wang, P. Liu, H. Jiang, Z. Xu, Z. Ma, S. Oren, E.K. Chow, M. Lu, Tunable optical nanoantennas incorporating bowtie nanoantenna arrays with stimuli-responsive polymer, Sci. Rep. 5 (2015) 18567.
[42] Y. Zhou, Y. Cai, X. Hu, Y. Long, Temperature-responsive hydrogel with ultra-large solar modulation and high luminous transmission for "smart window" applications, J. Mater. Chem. 2 (33) (2014) 13550–13555.
[43] BS EN 410:2011, Glass in building – determination of luminous and solar characteristics of glazing, in: Determination of Characteristics, 2011.
[44] A.C. Gladen, J.H. Davidson, S.C. Mantell, Selection of thermotropic materials for overheat protection of polymer absorbers, Sol. Energy 104 (2014) 42–51.
[45] M.F. Modest, Radiative Heat Transfer, Academic press, 2013.
[46] C.A. Gueymard, Spectral effects on the transmittance, solar heat gain, and performance rating of glazing systems, Sol. Energy 83 (6) (2009) 940–953.
[47] A. Mazhar, D.J. Cuccia, T.B. Rice, S.A. Carp, A.J. Durkin, D.A. Boas, B. Choi, B. J. Tromberg, Laser speckle imaging in the spatial frequency domain, Biomed. Optic Express 2 (6) (2011) 1553–1563.
[48] O.Z. Sharaf, M.F. Orhan, Concentrated photovoltaic thermal (CPVT) solar collector systems: Part I–Fundamentals, design considerations and current technologies, Renew. Sustain. Energy Rev. 50 (2015) 1500–1565.
[49] Q. Xuan, G. Li, Y. Lu, B. Zhao, X. Zhao, Y. Su, J. Ji, G. Pei, Overall detail comparison for a building integrated concentrating photovoltaic/daylighting system, Energy Build. 199 (2019) 415–426.